Draft version April 20, 2022
Typeset using LaTeX **twocolumn** style in AASTeX63

Tracking a beam of electrons from the low solar corona into interplanetary space with the Low Frequency Array, Parker Solar Probe and 1 au spacecraft.

Samuel T. Badman,[1,2] Eoin Carley,[3] Luis Alberto Cañizares,[3,4] Nina Dresing,[5] Lan K. Jian,[6] David Lario,[6] Peter T Gallagher,[3] Juan C. Martínez Oliveros,[2] Marc Pulupa,[2] and Stuart D. Bale[1,2]

[1] *Physics Department, University of California, Berkeley, CA 94720-7300, USA*
[2] *Space Sciences Laboratory, University of California, Berkeley, CA 94720-7450, USA*
[3] *Astronomy & Astrophysics Section, Dublin Institute for Advanced Studies, D02 XF86, Ireland.*
[4] *School of Physics, Trinity College Dublin, Dublin 2, Ireland.*
[5] *Department of Physics and Astronomy, University of Turku, Finland*
[6] *Heliophysics Science Division, NASA Goddard Space Flight Center, Greenbelt, MD 20771, USA*

Submitted to ApJ

ABSTRACT

Type III radio bursts are the result of plasma emission from mildly relativistic electron beams propagating from the low solar corona into the heliosphere where they can eventually be detected *in situ* if they align with the location of a heliospheric spacecraft. Here we observe a type III radio burst from 0.1-16 MHz using the Parker Solar Probe (PSP) FIELDS Radio Frequency Spectrometer (RFS), and from 10 - 80 MHz using the Low Frequency Array (LOFAR). This event was not associated with any detectable flare activity but was part of an ongoing noise storm that occurred during PSP encounter 2. A deprojection of the LOFAR radio sources into 3D space shows that the type III radio burst sources were located on open magnetic field from 1.6-3 $R_\odot$ and originated from a specific active region near the East limb. Combining PSP/RFS observations with WIND/WAVES and Solar Terrestrial Relations Observatory (STEREO)/WAVES, we reconstruct the type III radio source trajectory in the heliosphere interior to PSP's position, assuming ecliptic confinement. An energetic electron enhancement is subsequently detected *in situ* at the STEREO-A spacecraft at compatible times although the onset and duration suggests the individual burst contributes a subset of the enhancement. This work shows relatively small-scale flux emergence in the corona can cause the injection of electron beams from the low corona into the heliosphere, without needing a strong solar flare. The complementary nature of combined ground and space-based radio observations, especially in the era of PSP, is also clearly highlighted by this study.

Keywords: Sun, radio, electrons

1. INTRODUCTION

Type III radio bursts are the characteristic signature of beams of energetic electrons injected by transient processes in the solar corona onto interplanetary magnetic field (IMF) lines first classified from solar impulsive emission by Wild & McCready (1950). As the electron beams propagate away from the Sun, they produce Langmuir waves (L) which mode convert (via one of several possible processes, e.g. Melrose 2017) to radio emission at approximately the local electron plasma frequency (f_{pe}) or its second harmonic. As the electron plasma frequency is proportional to the square root of the electron plasma density (n_e) which decreases with the distance from the Sun, type III bursts are readily identified in radio spectrograms as transient signals dropping in frequency with time with a characteristic timescale of minutes to hours (Wild & McCready 1950). This frequency ranges from $\mathcal{O}$(100 MHz) in the lower corona down to $\mathcal{O}$(10 kHz) at $\sim$1 au. The coronal plasma frequencies are readily observed and imaged by ground based observatories. Around 10-15 MHz, the

Corresponding author: Samuel T. Badman
samuel_badman@berkeley.edu

burst passes below the typical cut-off frequency of the Earth's ionosphere and therefore can only be detected by space-based radio antennas.

Further, this radio emission is widely beamed (e.g. Lecacheux et al. 1989; Bonnin et al. 2008) and very luminous, meaning emission from the same event can be detected not just by Earth-based observatories, but also by widely separated spacecraft in the inner heliosphere. Additionally, the electron beam itself can survive out beyond 1 au and provide additional *in situ* information of the burst such as near-relativistic electron intensity enhancements (e.g. Ergun et al. 1998) or direct detection of Langmuir waves (e.g. Gurnett & Anderson 1976). For further context, Reid & Ratcliffe (2014) present a relatively recent review on type III burst properties and current theoretical understanding of the phenomena.

Type III radio bursts therefore produce a wide variety of diagnostic information about themselves and the ambient properties of the heliosphere such as the radial evolution of the solar wind plasma density and magnetic topology of the IMF lines. However, much of this information requires obtaining knowledge about the burst's trajectory through the interplanetary space. For example, the electron beam trajectory traces open field lines starting low in the corona all the way out into interplanetary space. They therefore can be a passive tracer of both open coronal magnetic field (important for solar wind acceleration studies) and over larger scales in the heliosphere where the magnetic field forms the channels along which space weather events are guided. Additionally, since the emission frequency is directly related to the local plasma frequency and therefore plasma density, an accurate trace of the burst provides a trace through the density structure of the heliosphere allowing testing or development of density models (the latter of which was done by Leblanc et al. 1998). Further, since emission of type III radio emission occurs near the local plasma frequency, electromagnetic dispersion of the emitted waves is important. This means that propagation of the radio waves is affected by density variations, both through large scale gradients and by small scale inhomogeneities. For example, if a radio emission is formed in a localized pocket of reduced plasma density surrounded by overdense regions, the radiation would not propagate through the overdense regions and so it would not be detected by widely separated spacecraft. Smaller scale density fluctuations also lead to random walks of photons before they escape to free stream. Measurements of apparent source size and source height allow these fluctuations to be quantified both in coronal contexts (Kontar et al. 2019) and in the heliosphere (Krupar et al. 2020; Musset et al. 2021).

In this work we combine multiple observational signatures of a single type III radio burst observed by three well-separated spacecraft as well as ground-based telescopes during the outbound phase of the second solar encounter of NASA's Parker Solar Probe (PSP; Fox et al. 2016) on 2019 April 9. We combine these observations in an effort to track the injection and escape from the corona of the electrons responsible for the type III burst, the interplanetary trajectory of those electrons, and their *in situ* signature at ∼1au. In section 2 we introduce the various data sources and observations used in the project. The relative positions of these observing spacecraft and instruments are depicted in figure1. In section 3 we discuss the different methods used to probe the type III's behaviour on its journey out from the Sun. In particular, we focus on ground based radio imaging of the burst in the outer corona (section 3.1), time-of-flight analysis between different heliospheric spacecraft to probe the burst's trajectory in the inner heliosphere (section 3.2), and finally study *in situ* signatures of the electron beam arrival at the Solar Terrestrial Relations Observatory A (STEREO A; Kaiser 2005) at 1 au (section 3.3). In section 4, we summarize the results from combining these different sets of observations. Lastly, in section 5 we discuss the implications and novelty of our results and future opportunities for collaborative studies between ground and space-based radio observatories and other supporting instrumentation.

2. OBSERVATIONS AND DATA SOURCES

While PSP launched in an extremely quiet solar minimum, its second solar encounter in late March and April 2019 occurred during a wealth of solar radio activity with hundreds of individual type III bursts detected over this interval (Pulupa et al. 2020). During this time, at least two active regions (ARs) were potentially contributing to this activity (AR 12738; Krupar et al. 2020; Cattell et al. 2020) and (AR 12737; Harra et al. 2021). In this work, we focus on a particular, well isolated Type III burst observed on 2019 April 9. The radio context for this day as observed by the FIELDS Radio Frequency Spectrometer (FIELDS/RFS; Bale et al. 2016; Pulupa et al. 2017) on board PSP is shown in Figure 2 with the individual burst of interest indicated by a red box around 12:40 UT. Clearly, it is one of many bursts on this day and not the most intense however it presents the advantage of being an isolated single burst observed by multiple spacecraft and ground based instrumentation.

On 2019 April 9 the NOAA AR 12738 was located near the east limb of the sun (N06^{o}E48^o at ∼18:00 UT and high magnetic flux density extending at least 10^o further eastwards, see Figure 3). At

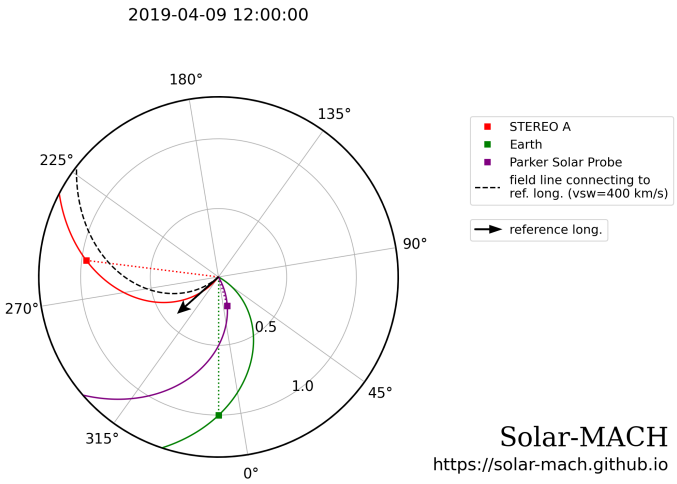

Figure 1. Instantaneous ecliptic positions of the spacecraft constellation used in this work at 12:00 UT on 2019/04/09, expressed in Stonyhurst coordinates (Sun-Earth line at 0^o longitude). Each spacecraft is connected back to the Sun by a 400 km/s reference Parker spiral. A black arrow and black dashed Parker spiral indicates the longitude and nominal trajectory of emission from AR 12738, the likely origin of the burst in this work. Note the "Earth" location is a proxy for the locations of the Wind/WAVES, GOES-15/XRS and LOFAR instruments, all used in this work. Figure generated using https://solar-mach.github.io

this time AR 12737 was near the west limb and decaying rapidly. The soft X-ray 1-8 Å flux measured by the GOES X-ray sensor (XRS, Chamberlin et al. 2009) showed very small levels of activity, with only B-class flares observable within the time range of our event of interest. The radio and X-ray observations are depicted in Figure 4 with panels (a-d) respectively showing radio spectrograms observed by Wind/WAVES, STEREO A/WAVES, PSP/FIELDS/RFS. The bottom panel zooms out to a longer time interval and shows GOES X-ray fluxes which are largely featureless both at the time of the burst and in the preceding and following hours. At 12:45 UT a type III radio burst was observed in the dynamic spectra from the Low Frequency Array (LOFAR, van Haarlem et al. 2013) from 10-90 MHz and STEREO-A/WAVES (S/WAVES, Bougeret et al. 2008) and WIND/WAVES (Bougeret et al. 1995) from 0.4-14 MHz (Figure 4a-b, and 4d). The same type III was observed by the PSP/FIELDS/RFS instrument 6 minutes earlier, due to its closer proximity to the sun during the event (timeshift applied in the plot, Figure 4c). The relative positions and nominal magnetic connectivity of the different spacecraft relative to the reference longitude of the source active region is indicated in Figure 1. Comparing the radio and X-ray data, this radio burst was not well associated with any significant flaring activity and was likely related to an ongoing noise storm associated with AR 12738.

LOFAR observations of the type III from 10-90 MHZ allow its emergence in the lower corona to be tracked out to ∼3 $R_\odot$ (section 3.1). The observations of the same type III radio burst by PSP, STEREO-A and WIND provide the opportunity to localise the position of this radio burst further out into the inner heliosphere and associate it with a given IMF line. *In-situ* observations of energetic electrons by the STEREO A Solar Electron and Proton Telescope (SEPT; Müller-Mellin et al. 2008) and lower energy electrons by the STEREO-A Suprathermal Electron instrument (STE; Lin et al. 2008) suggest the burst electrons from this type III burst can be tracked from its origin, low in the corona at AR 12738, far into the heliosphere all the way to STEREO-A (see Figure 1). An energetic electron enhancement of solar origin was indeed detected at STEREO A at compatible times, although as discussed in section 4, we do not conclusively isolate the individual contribution of this burst from the overall population produced by the ongoing noise storm.

3. METHODS

3.1. *Imaging and deprojection of LOFAR radio sources*

During PSP encounter 2 the 36 core + remote stations of the LOFAR-provided interferometric observations of the sun, generating imaging spectroscopy observations in the range of 10-90 MHz (the remainder of the international array was also used to perform beam-formed observations of interplanetary scintillation during this observing period). A dynamic spectrum of the type III radio burst observed by LOFAR is shown in Figure 4(d). LOFAR interferometric data was calibrated (from simultaneous observaions of Tau A) and processed using the Default Preprocessing Pipeline (DPPP; van Diepen et al. 2018) followed by an implementation of w-stacking clean (WSClean; Offringa et al. 2014) to produce images with a cadence of 1.67 seconds. Images at seven frequencies from ∼20-80 MHz are displayed in Figure 5a, showing radio sources overplotted on an AIA 171 Å image and a potential field source surface (PFSS) magnetic field extrapolation using pfsspy (Stansby et al. 2020) and data from the Global Oscillation Network Group project (GONG; Harvey et al. 1996). The time of the GONG magnetogram used for the extrapolation was 13:04 UT, on April 9th 2019, with a source surface radius of 2.5 $R_\odot$. The type III radio sources clearly emanate from AR 12738 along the negative open field to the south of the active region.

In order to determine the location of the type III radio burst sources with respect to the parent active region,

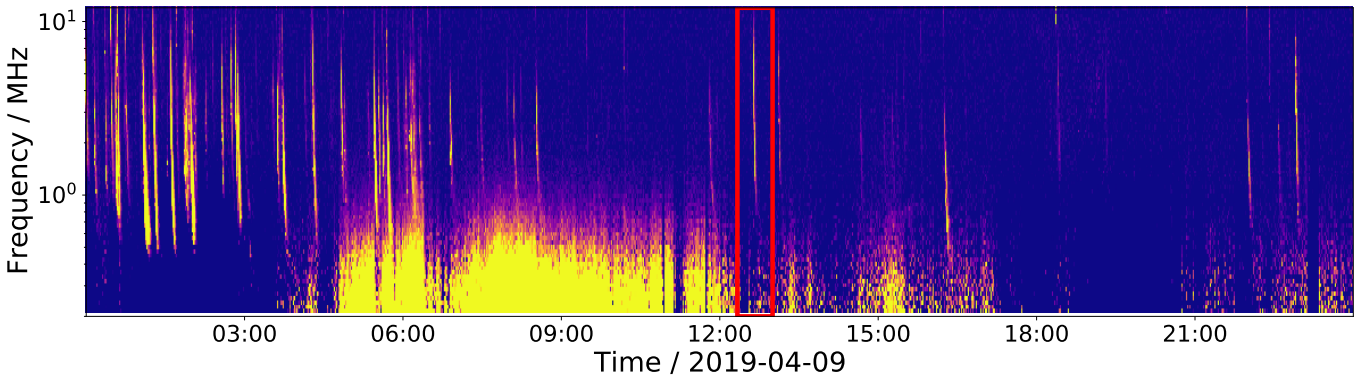

Figure 2. PSP/RFS radio spectrogram for 2019 April 9th. Each vertical stripe is a Type III burst. The ∼12:40 UT burst studied in this paper is indicated by the red box annotating the figure. The broadband signatures at lower frequencies are due to variations in the in situ electron plasma parameters (Moncuquet et al. 2020; Liu et al. 2021)

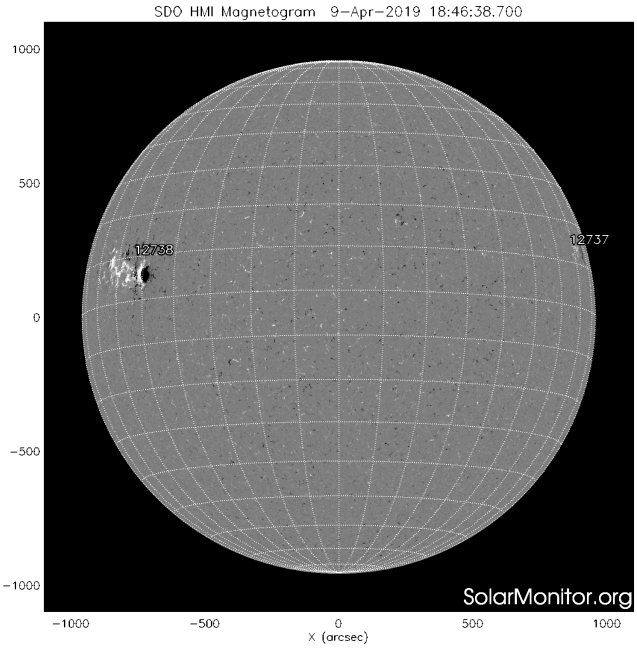

Figure 3. HMI magnetogram showing AR 12738 located near the east limb of the sun (48°E). During PSP encounter 2, this AR was associated with a long-duration radio noise storm in which continuous type III activity was observed (Pulupa et al. 2020; Krupar et al. 2020; Cattell et al. 2020)

a basic deprojection using the Newkirk density model (Newkirk 1961) was performed. We assume the type III emission is from harmonic emission in an atmosphere described by a coronal density model where the sources are located at a height of r_{model}. Their distance from the plane of sky (POS) is then $z = \sqrt{r_{model}^2 - r_{pos}^2}$, where r_{pos} is the height of the radio sources on the POS. Although it is a rudimentary deprojection, it places the type III radio burst sources where we would expect them, in an open field region (from a PFSS model) accessible to an active region , see Figure 5.

The angle from the sky-plane of the type III burst roughly matches where the interplanetary type III is located from PSP-SWAVES-WAVES time-of-flight analysis (section 3.2, below). A few caveats are noted however: (i) the deprojection uses an arbitrary, and spherically symmetric, density model (one of many possibilities), so gives only a rough indication of the source positions, (ii) the radio sources are also large at these frequencies, the sizes of the green spheres in the 3D plot are 1-sigma from a Gaussian fit to the sources in the LOFAR images.

3.2. *Time-of-flight using PSP, STEREO and Wind*

As noted above, this burst was also observed at frequencies below ∼14 MHz in the three space-based radio instruments S/WAVES, Wind/WAVES and PSP/FIELDS (see Figure 4). At these frequencies, the burst is travelling over interplanetary distances and thus the length scales of the trajectory and variation in light travel time to the different observers are on the order of light minutes. Radio waves at these frequencies do not penetrate the Earth's ionosphere so direct interferometric imaging is not available with current space-based instrumentation.

However, all the above instruments produce dynamic spectrum with a cadence of $\lesssim$1 minute (60s for Wind/WAVES, ∼38s for S/WAVES and ∼7s for PSP), and on the date of this case study were all located multiple light minutes apart. Thus, the light travel time from the burst to the different spacecraft can be significantly different and, critically, measurable. With the assumption of straight line propagation from a unique source position to each spacecraft, the difference in time of arrival at a given frequency between different spacecraft can be used to make a simple geometric reconstruction of the most likely source position (see Alcock (2018) and Appendix 1). With this method and a constellation

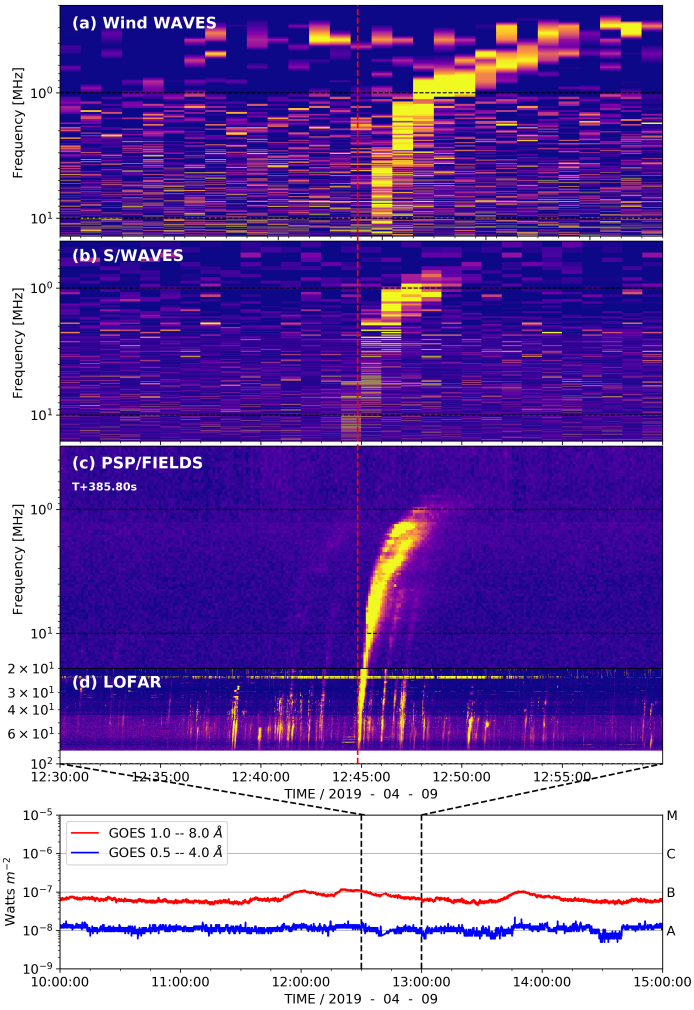

Figure 4. A type III radio burst observed with (a) WIND/WAVES, (b) STEREO-A/WAVES (S/WAVES), (c) PSP/FIELDS and (d) LOFAR. The radio burst is observed at LOFAR, S/WAVES and WIND/WAVES at ∼12:45 UT as they are all located at a distance of ∼1 au from the Sun, while it was observed 6 minutes earlier by PSP due to its closer proximity to the sun at $\sim 50 R_{\odot}$. Using a PSP-Earth light travel time, PSP's dynamic spectra has been shifted by +385.80s to match the one of LOFAR. Visual confirmation shows a match of the bright and fainter bursts. An additional zoom out panel shows GOES X-ray flux for several hours either side of the burst in energy channels 0.5-4.0∼ $\AA$ (blue) and 1.0-8.0∼ $\AA$ (red), demonstrating the lack of strong flare events associated with these bursts.

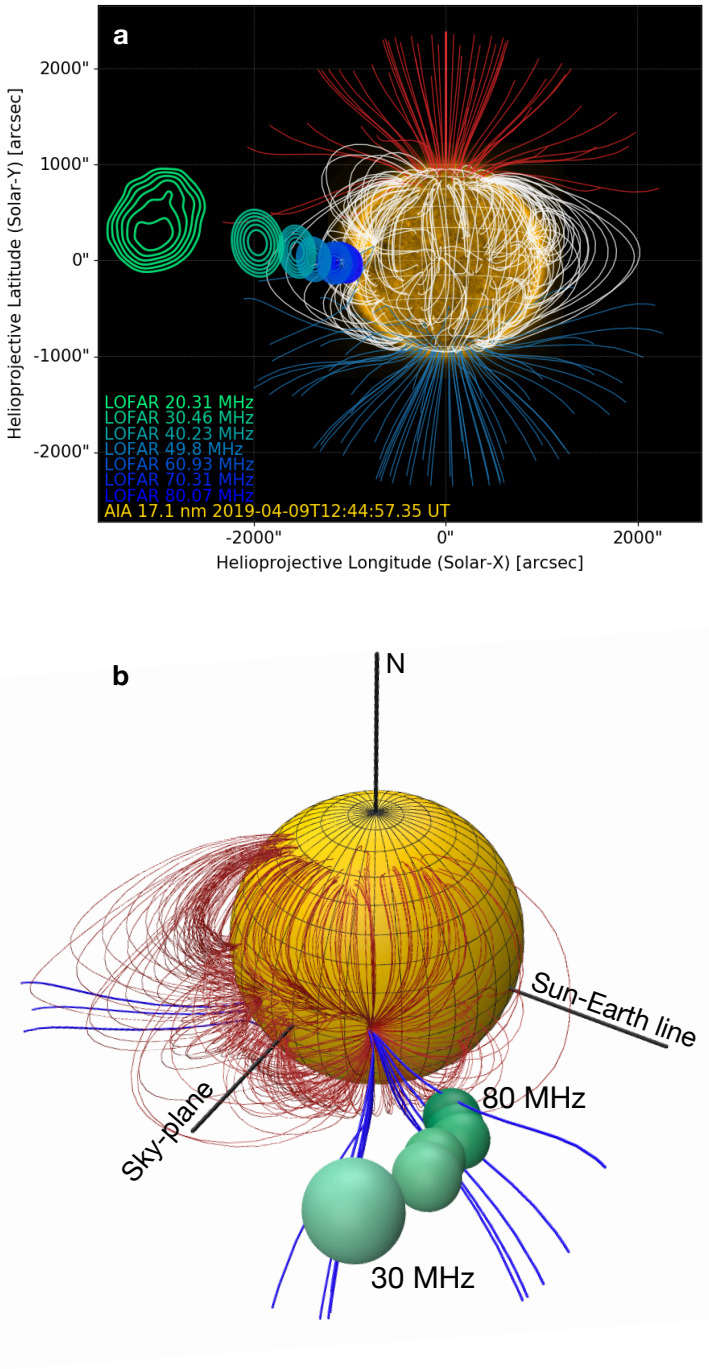

Figure 5. (a) Type III radio burst sources observed by LOFAR from 20-80 MHz overlaid on a PFSS magnetic field extrapolation using GONG. The type III sources emanate from the active region near the east limb and are situated close to the negative open magnetic field rooted in the active region. (b) A deprojection of the radio sources using a Newkirk density model (Newkirk 1961), assuming emission at the second harmonic of the local plasma frequency. This places the radio sources on the open field lines ∼40° beyond the east limb. This agrees well with the trajectory of the radio sources in Figure 6

.

of three well-separated instruments, the position may only be confined uniquely in 2D and so we make the assumption that the source is approximately located in the ecliptic plane, which is supported by the near-equatorial parent active region and associated coronal open field lines (Figure 5), and complementary localization efforts by Krupar et al. (2020).

The result of such a reconstruction as a function of frequency for the burst studied in this paper is depicted

in Figure 6. The implementation procedure is detailed in appendix 1. The top panel of Figure 6 provides an overview of the whole inner heliosphere, depicting the spacecraft constellation triangle consisting of PSP, Wind and STEREO-A, as well as the burst reconstruction coloured from light to dark as it drops in frequency and moves out from the sun. The solid markers indicate the positions corresponding to the central value of the measured time delays, while the diffuse cloud indicates the uncertainty in position obtained by varying the measured time delay within the time resolution of the instruments. Two dotted lines indicate Parker spirals initiated at 30°E and 60°E relative to the central meridian with solar wind speed of 400 km s^{-1}, informed by *in situ* measurements at STEREO-A at this time. These show that it is plausible that energetic electrons injected in the vicinity of these interplanetary field lines would reach STEREO-A (Section 3.3).

The bottom panel of Figure 6 zooms in on the reconstructed type III trajectory and uncertainty region. Red dots close to the origin indicate the source positions as reconstructed by LOFAR (Section 3.1) and plotted in the ecliptic plane. This shows the two methods agree very well with the directivity of the burst onto field lines associated with AR 12738 and which intersect the orbit of STEREO-A. It also shows directly that the burst moves outwards from the sun as it drops in frequency.

It is worth noting the time delay generated trajectory implies the burst has been tracked out to 40 $R_\odot$. However, the lowest frequency observed at PSP is only 800 kHz for which typical density models (e.g. Leblanc et al. 1998) would suggest the outer radius at which emitted radiation reaches PSP is only ∼10 $R_\odot$ (20 $R_\odot$) for fundamental (harmonic) radiation. This implies (as previously noted e.g. by Steinberg et al. 1984; Thejappa & MacDowall 2010; Thejappa et al. 2011) that refractive effects on the radio wave propagation likely affect the arrival time, at least near the emission site where the local plasma frequency and radio frequency are similar. Kontar et al. (2019) have shown at coronal distances that density scattering can result in the apparent type III source radii appearing at higher altitude than their true location with a correction of the order of the distance itself (i.e. for heliospheric altitudes this would correspond to 10s of solar radii consistent with the observed discrepancy in the present work). Krupar et al. (2018) and Krupar et al. (2020) have shown such density fluctuations are of fundamental importance in understanding the shape of the time profiles of type III bursts in the inner heliosphere. As such, the burst trajectory produced here is likely a "lensed" version of the true trajectory for which the true radii are smaller. A detailed analysis of these propagation effects on the time-of-arrival localization technique will be the subject of future work, but we note the work of Kontar et al. (2019) suggests the lensing is primarily a radial shift and that the directivity of the burst trajectory remains reliable.

For this case study we are therefore confident that the correspondence between the coronal and interplanetary localization indicates the true path of the burst in escaping the corona onto open field lines. Further, the directivity and association with AR 12738 is consistent with localization performed by Krupar et al. (2020) where the authors use a different but complementary triangulation technique on a burst 6 days earlier (April 03 2019) when AR 12738 was behind the East limb. They place this burst within 30 degrees of the ecliptic plane, which would suggest a small correction (∼10%) in light travel time to our ecliptic propagation assumption. With the direct imaging from LOFAR placing the burst studied here near the ecliptic we argue this is a good approximation for our burst. The combination of the localization of Krupar et al. (2020) with our work strengthens the inference of the source and evokes a picture of an individual active region rotating with the sun and injecting type III bursts into different regions of the interplanetary space with time.

Lastly, Figure 4 shows clearly that the burst continues to propagate beyond the maximal triangulated distance, since radio emission is observed in Wind and STEREO-A at frequencies below the lowest frequencies observed by PSP. This suggests the beam reaches regions where the local plasma frequency is below the in situ plasma frequency at PSP, so radio emission cannot propagate inwards towards PSP. Thus it is plausible that electron beams along these mapped field lines can make it out to reach STEREO-A at 1 au.

3.3. *In-situ analysis*

As mentioned in the previous section, Figure 6 shows that the magnetic connection along nearby Parker spiral field lines would allow the potential *in situ* detection by STEREO-A of the electrons produced during the solar eruption origin of the type III emission, although the exact nominal 400 km/s connection of STEREO A would be westward of the AR (see Figure 1).

We have analyzed energetic electrons measurements from the SEPT and the Solar Wind Electron Analyzer (SWEA; Sauvaud et al. 2008) instruments on board STEREO-A to determine whether such electrons were detected. We further contextualize the *in situ* environment around the spacecraft at this time with magnetic field measurements from STEREO-A/IMPACT/MAG (Acuña et al. 2008) and thermal plasma measurements

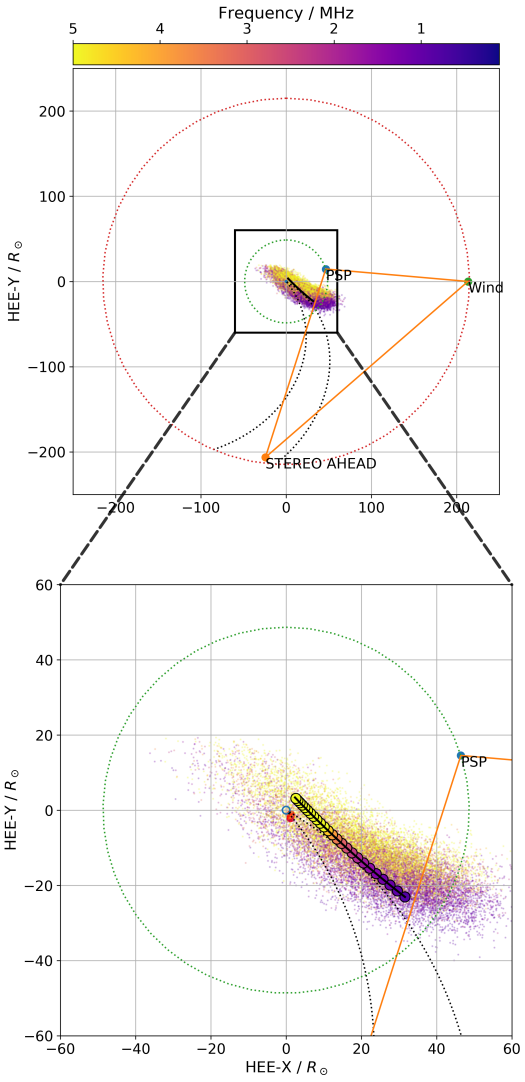

Figure 6. Triangulation of type III radio burst trajectory in the inner heliosphere, shown in the ecliptic plane. The positions are from a time-of-flight method to PSP, WIND and STEREO-A, the locations of which are indicated. The solid markers represent the central value, while the diffuse cloud shows the position uncertainty due to the impact of the instrument time resolution on the time-of-flight measurement. The color of the burst trajectory indicates the measured frequency at a given position. The bottom panel zooms in on the burst down to PSP's radius allowing both the time delay derived trajectory and LOFAR imaging results (red scatter points) to be compared. The dotted lines indicate Parker spirals generated for 400 km/s solar wind starting at 30°E and 60°E relative to the central meridian. The faint blue and red dotted circles depict the heliocentric distances of PSP ($\sim 50R_{sun}$) and of 1 au, respectively. The coordinate frame is Heliocentric-Earth-Ecliptic (HEE) with the sun at the origin, Earth located along the x-axis and the x-y plane is the ecliptic (Earth's orbital plane).

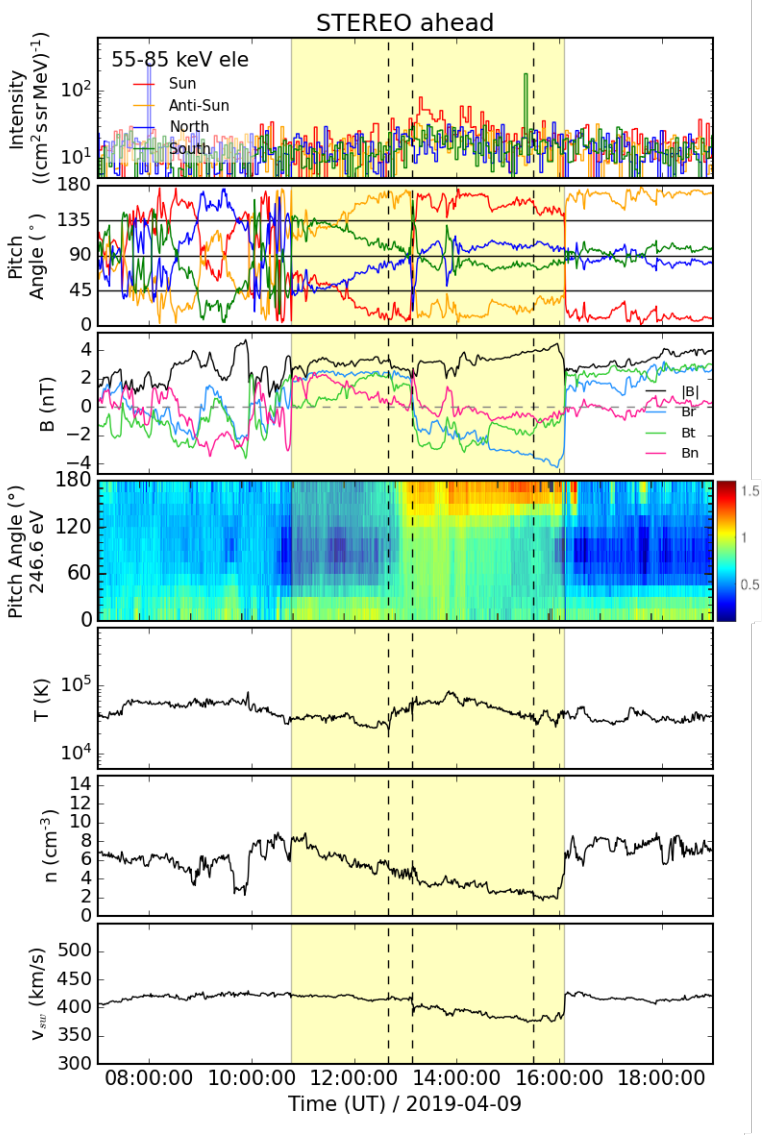

Figure 7. *In situ* observations by STEREO-A on 2019 April 9. From top to bottom: 55-85 keV electron intensities measured by the four telescopes of the STEREO/SEPT instrument, pitch angles scanned by the central axes of these four-telescopes, magnitude and components of the magnetic field vector in the spacecraft-centered RTN coordinate system, pitch angle distribution of suprathermal electrons at 246.6 eV (color for the logarithm of phase space density), solar wind proton temperature, density, and speed. The yellow shaded period, the same as the one marked in Fig. 10, indicates a period with peculiar field direction studied in detail.

from SWEA. SEPT consists of two dual double-ended particle telescopes which measure electrons in the energy range of 40–400 keV. The four apertures of SEPT were termed Sun, Anti-Sun, North, and South owing to their looking directions along the nominal Parker spiral direction in the ecliptic plane (Sun and Anti-Sun) and perpendicular to the ecliptic plane (North and South). In the original configuration of the STEREO-

A spacecraft, the longitudes of the central axis of the Sun and Anti-Sun apertures in the spacecraft-centered Radial-Tangential-Normal (RTN) coordinate system were $\phi_{Sun}\sim135°$ and $\phi_{Asun}\sim-45°$, respectively, designed to align with the nominal Parker Spiral azimuthal angle at 1 au. However, after the STEREO-A superior conjunction with Earth in early 2015, the spacecraft changed orientation resulting in the Sun and Anti-Sun apertures still pointing in the ecliptic plane but now *perpendicular* to the nominal Parker spiral direction, with $\phi_{Sun}\sim-135°$ and $\phi_{Asun}\sim45°$, respectively.

On 2019 April 9, a small electron intensity enhancement at energies below ∼100 keV was observed by STEREO-A/SEPT close to the emission time of the Type III burst studied in the previous section. Figure 7 summarizes the *in situ* context at the location of STEREO-A at the relevant times. In the top panel, we see timeseries of 55-85 keV electron intensities measured by the different apertures of SEPT. The onset of the electron event is most clearly seen in the "Sun" aperture (red trace, top panel) and occurred after ∼12:40 UT (first dashed line). A current sheet crossing indicated by the magnetic field orientation changing to $\phi \sim -135°$ occurred at ∼13:08 UT (second dashed line) when electron intensities were still increasing. Electron intensities reached a maximum at about ∼13:30 UT, and slowly decreased to pre-event intensities at about ∼15:00 UT. Throughout all this period, the magnetic field lay close to the ecliptic and perpendicular to the nominal Parker spiral field direction, which makes the post-superior-conjunction orientation of the Sun and Anti-Sun apertures of SEPT ideal for the detection of these electrons. Prior to the current sheet, the ecliptic component of the field was oriented at 45^o in the RTN coordinate system, and then flipped 180^o to point at -135^o. The entire interval of this "perpendicular-to-Parker" interval is captured by the yellow box superimposed on the different panels. The current sheet crossing happens approximately halfway through this interval.

The second panel of Figure 7 shows the angle between the instantaneous magnetic field direction (RTN components shown in the third panel of the figure) and the central axis of each one of the SEPT apertures; the orange and red trace's close alignments with 0° and 180° indicate the favorable orientation of the instrument apertures for detecting particles propagating along the magnetic field, with the two traces switching places at the current sheet crossing.

The fourth panel down presents the pitch angle distribution of suprathermal electrons at 246.6 eV as measured by SWEA. Prior to the current sheet crossing, the pitch angle distribution (defined relative to the local field orientation) is anisotropic and peaked at 0^o indicating it is parallel to the field lines. After the current sheet crossing, the distribution is peaked at ∼180° i.e. antiparallel to the field lines. Given the field orientation has flipped 180^o, this indicates the dominant direction of the suprathermals remains consistent and at all times is flowing into the direction of the SEPT "Sun" aperture. After the current sheet and coincident with the peak in 55-85 keV electrons, the suprathermal electrons do become more isotropic (but still clearly single-peaked); this pitch angle spread decays away on the same timescale as the energetic electron population decreases to background levels.

We note the pitch angle distributions of the 246.6 eV electrons are consistent with the arrival direction of the energetic electrons (flowing into the SEPT "Sun" aperture. This suggests the field lines at STEREO A at this time are open (1 footpoint connecting to the Sun) and, since the energetic electrons arrive *from* the direction of this footpoint, they are likely of solar origin.

Finally, plasma temperature, density and radial flow speed are shown respectively in the latter three panels of Figure 7. The lack of sharp changes in any of these quantities during the energetic electron enhancement indicates there is no evidence that the electrons are a local enhancement due to interplanetary processes such as shock acceleration, but instead supports a solar origin. This is further supported by longer term *in situ* context described in appendix 2 from which we see there was no SIR or CME candidate close enough in time to source the energetic electrons measured, and that the background solar wind stream likely had a distinct solar source evidenced by a peak in solar wind Fe charge states.

The unusual magnetic field orientation observed during this electron event raises questions about the interplanetary context under which this event occurred. Specifically, the electron event occurred during the passage of a peculiar structure with magnetic field orientation perpendicular to the nominal Parker containing a current sheet crossing which rules out the simplest picture of a single Parker spiral field line connecting STEREO-A back to the active region source of the Type III burst.

A 55 keV (85 keV) electron would take about ∼23 (∼ 19 minutes) to travel a distance of 1.2 au along a nominal Parker spiral for a spacecraft located at 1 au from the Sun. For an observer located at 0.967 au like STEREO-A, a 55 keV (85 keV) electron would take about ∼18 (∼ 15 minutes) to travel the radial distance from the Sun to the spacecraft. The actual path followed by these electrons before reaching STEREO-A when embedded

in this structure, as well as how this structure modified the STEREO-A magnetic connection with the Sun, are uncertain. This means mapping arrival time of the event at STEREO-A back to a specific emission from the Sun is difficult, although the nominal Parker spiral delays quoted above are likely to represent a lower bound on expected time delays.

We note that the first radio waves associated with the type III radio burst were detected by LOFAR at 12:45 UT implying a release time in the low corona of ∼12:37 UT. This appears too late therefore to explain the initial onset time of the energetic electrons observed in situ by STEREO-A/SEPT at ∼12:40 UT. Moreover, the timescale of the whole enhancement tracked by SEPT is of order 1-2 hours, significantly longer than the timescale of any given burst, suggesting multiple bursts could be contributing to the population. However, the anisotropic electron enhancement which continued during the current sheet passage at 13:08 UT and the subsequent electron intensity peak at ∼13:30 UT are compatible with electrons injected during the type III radio burst analyzed in Section 3. This suggests that although the burst likely can't explain the entire enhancement it contributes part of the population during the rise in energetic electron population level. The anisotropy in electron strahl throughout this interval, lack of shock or other CME candidate events at compatible times, and other evidence presented above and in appendix 2, suggest that the enhancement is an electron beam of solar origin, and the Parker spiral connection of STEREO at this time points to the same AR that produced the type III burst as the likely origin. The "perpendicular-to-Parker" field configuration makes the picture somewhat more challenging to sketch but a plausible scenario and schematic is presented in section 5 below.

4. RESULTS

Here we summarize the results of our multi-instrument anaylsis tracking a case study of a single well isolated type III radio burst from its emission onto open field lines by a source active region, its propagation through the corona and out into interplanetary space and lastly, its possible association with *in situ* measurements from the STEREO-A spacecraft near 1 au.

Following on from Pulupa et al. (2020), we investigated an interval of significant radio activity that occurred during the second encounter of PSP in April 2019 (see Figure 2). Among hundreds of type III bursts, we identified an individual well-isolated case study which was observed in 1 au dynamic spectra corresponding to coronal altitudes at 12:45 UT on April 9 2019. The burst was clearly identifiable at interplanetary frequencies with plausible time delays by widely separated interplanetary spacecraft (Figure 4), specifically PSP at $50R_{\odot}$, Wind/WAVES at the Earth-Sun L1 Lagrange point, and by STEREO A/WAVES at 1 au, at slightly more than 90 degrees from the Earth-Sun line (see Figure 1).

Using radio imaging with the Low Frequency Array from $20 - 80$ MHz and a simple deprojection analysis assuming a Newkirk coronal electron density model (Newkirk 1961), the burst was placed in 3D space at coronal altitudes at longitudes clearly associated with AR 12738 located at N06^{o}E48^o in helioprojective coordinates on April 9, 2019 (Figure 3). This was consistent with the association of the overall type III activity on these dates made by Pulupa et al. (2020); Krupar et al. (2020); Cattell et al. (2020). The imaging showed the burst increasing with altitude with decreasing frequency and the deprojection placed it in a region of open magnetic field lines in the vicinity of the relevant active region (Figure 5). GOES/XRS measured X-Ray radiation over this time which indicated that there was no significant flaring component associated with the injection of the burst (Figure 4).

Having established the burst to be injected onto open field lines and therefore expected to reach interplanetary space, we investigated the source propagation out to several 10s of solar radii using a novel time delay technique (see appendix 1) leveraging the multi-light minute separation between different heliospheric spacecraft with radio spectra instrumentation (PSP, Wind and STEREO-A). This analysis yielded a trajectory for the burst at frequencies from 10 MHz down to 800 kHz at which point the radio frequency became evanescent along paths to PSP (this means the burst propagated beyond the heliocentric distance of PSP). The derived trajectory showed the burst to be increasing in distance from the Sun with decreasing frequency, and to be directed along a longitude consistent with the active region and coronal trajectory found by LOFAR. This consistency utilizes an error region from the analys computed by accounting for the limited time resolution of the individual instruments radio data products, most significantly that of Wind/WAVES for which the most accessible data product has a time resolution of 1 minute for each spectrum. The actual distances computed were larger than expected from typical interplanetary density models, which suggests scattering by density fluctuations at the emission location is an important effect which effectively lenses the burst and makes it appear to be sourced at higher altitudes (Kontar et al. 2019). This is discussed further in Section 5.

Lastly, motivated by the consistent longitude between the active region, LOFAR imaging, interplanetary triangulation, and Parker spiral field lines which mapped to the location of STEREO A, we examined in detail the signatures of energetic electrons at that spacecraft to determine if the electron beam was detected at 1 au. An energetic electron event was indeed observed at STEREO A at compatible times, although its true onset (12:40 UT) was too early to be explained by the specific burst studied here (emitted at approximately 12:37 UT).The duration of the electron enhancement (peaking at 13:30 UT) is compatible with the electrons that generated the type III radio burst arriving at STEREO-A during the rising phase of the 55-85 keV electron event and suggests they contribute to the peak of this electron event. Further, detailed *in situ* analysis of the solar wind stream that swept past STEREO A at this time demonstrated clear evidence that the energetic electrons measured were solar in origin and were not associated with any *in situ* electron energization processes. The magnetic field lines at the event time were perpendicular to the nominal Parker spiral direction, however since the suprathermal electron pitch angle distribution was singularly peaked at all times, the field lines were likely magnetically open and would be expected to connect in the vicinity of the active region of interest. We suggest therefore that the burst likely contributes to the population of energetic electrons measured by STEREO-A, but that the overall population was comprised of multiple type III ejections which were happening near continuously on this and preceding days and that STEREO-A only measures a subset controlled by a favorable stream configuration advecting over the spacecraft at this time. In section 5 we include a proposed schematic representation of the magnetic field configuration which could explain the *in situ* signatures.

5. DISCUSSION & CONCLUSION

Taken together, our results show a successful multi-instrument and multi-spacecraft analysis method which can be used to trace an individual type III burst from its emission source through the corona, into interplanetary space and assess its connection to in situ signatures at 1 au. While the power of combining these different measurements together is the key focus of this paper it is worth discussing the implications of the individual components of the analysis in their own right.

Starting from low in the corona, this study shows a clear example of injection of an electron beam propagating into interplanetary space from a non-flaring (no enhanced X-ray flux to within the GOES-15/XRT sensivity level) active region. From Figure 4, we see the bursts reaching interplanetary frequencies (i.e. bursts observed in panel (c) *and* panel(d)) are an extremely small subset of a number of other injections into the corona (all bursts in panel (d)). The lack of associated X-ray emission and numerous small bursts at coronal altitudes around our event suggest there is a continous process of magnetic flux emergence and reconnection happening low in the solar corona throughout this time interval which is constantly injecting energetic electrons onto coronal field lines. The burst studied in this paper is the only one in Figure 4 which is observed by radio instrumentation at 1 au (panels (a) and (b)) and is the brightest event seen in this time interval in both PSP and LOFAR. Several fainter events measured by PSP between 1-10 MHz (see panel c) are drowned out by noise in S/WAVES and Wind/WAVES suggest that more bursts leave the corona than are measured by 1 au. Although the burst being sufficiently bright to be observed at 1 au is a necessary condition for the analysis we perform here, this observation is worth motivating since the *in situ* analysis in this work suggests energetic electron beams might be being injected onto interplanetary field lines continuously and not just by the brightest bursts.

The LOFAR imaging and deprojection analysis of the burst showed the burst moving radially outwards along open field lines in the vicinity of the active region (AR 12738) that was suspected of producing the overal noise storm a priori. Additionally, the imaging yielded larger apparent source sizes with decreasing frequency as the burst propagated outwards, and this may encode information about the nature of coronal density fluctuations with increasing altitude. Given a type III electron beam producing electromagnetic radiation at or near the local plasma frequency, density fluctuations mean the emission can be refracted and reflected very strongly close to the source. Kontar et al. (2019) showed through modeling these fluctuations that the effect on the emitted radiation is to produce a surface of last scattering at higher altitudes and spread over a larger area than the area of the burst producing the emission. As discussed below, this effect is likely occurring in the interplanetary trajectory of the burst too. This shows that tracing type III electron beams in this way is not only useful for studying the phenomena themselves, but also the ambient medium through which they are traveling.

Continuing out into the inner heliosphere, the results from our time delay measurement demonstrate the power of a very simple analytical construction but also its limitations and possible convolution with heliospheric density structure. At the crudest level, our results demonstrate that the time delay of bursts observed at locations multiple light minutes apart does contain

real and non-trivial information about the trajectory of the burst at interplanetary length scales. In particular, we have obtained a directivity consistent with the source active region and deprojection analysis in the corona of the same burst. Further, we also see clearly that the burst propagates outwards over time as the frequency of emission decreases, in line with the canonical picture of type IIIs emitting radio waves near their local plasma frequency or harmonic from an outward propagating energetic electron beam.

However, we found that the distance this analysis places the burst at is too large to be explained by typical density models, even assuming harmonic emission. As discussed above, an inflated or "lensed" apparent source height is in line with the theoretical expectations of the effect of a power law of density fluctuations superimposed on a large scale spherically symmetric monotonically decreasing density model (Kontar et al. 2019). The mechanism described by Kontar et al. (2019) by which this effect occurs can be summarised as follows: When radio waves are emitted near the local plasma frequency of an inhomogeneous medium, the waves are strongly scattered by density variations and undergo a random walk. Waves that random-walk outwards (i.e. to larger heliocentric distances) gradually move into a medium with a lower plasma frequency due to the large scale density gradient. Eventually, they reach a point where they scatter one last time before being free to travel in straight lines. This process leads to a "surface of last scattering" from which radio waves propagate at straight lines. This means that when time delay (or direction finding) methods are used to localize the emission and assume straight line propagation, the rays point to this surface as the effective source, rather than the true emission location. Due to the radio waves needing to travel to higher altitudes to escape in this way, the effective source is necessarily further out than the true emission location, leading to the inflated source altitude.

Although this former work was performed at coronal altitudes, Krupar et al. (2018) and Krupar et al. (2020) have shown that the time profiles of type III bursts in a given frequency channel at interplanetary distances (in particular their exponential tail off) are consistent with a similar power law scattering process at work in the inner heliosphere. This suggests combining this time delay localization technique with density modeling is an interesting direction for future work which would result in being able to correct the trajectory while fitting amplitudes and power law slopes of density fluctuations, and potentially differentiating harmonic and fundamental radiation since the effect of scattering should be stronger on the latter type of emission. The corrected trajectory would also provide accurate measurements of the density variation in the inner heliosphere, and provide a direct tracing method for interplanetary field lines.

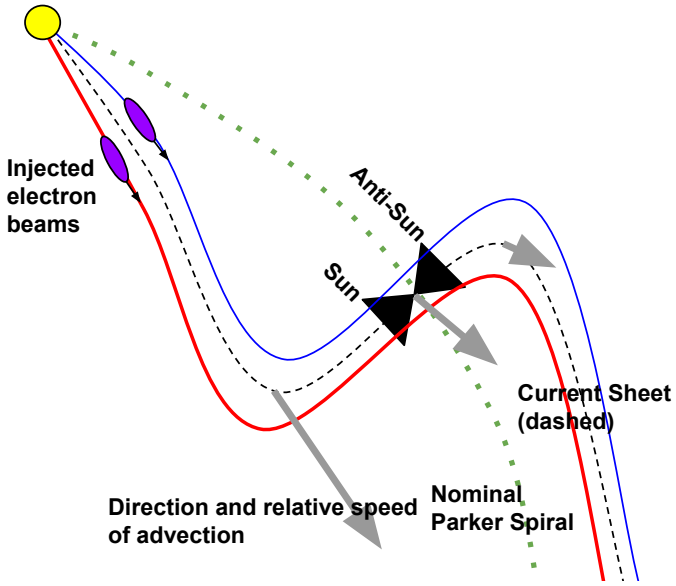

Figure 8. Schematic of the potential magnetic field configuration which advected over STEREO A during the time interval studied (yellow shading in Figure 7 and 10). STEREO A's location is marked by the 2 black triangles indicating the orientation of the SEPT Sun and Anti-Sun apertures which were oriented perpendicular to the Parker spiral direction. As noted in the main text, energetic electrons were observed in the Sun aperture. A proposed large "kink" in an other wise open magnetic field with two polarities (red and blue) are shown separated by a current sheet (blacked dashed curve). A yellow circle indicates the Sun where both field lines are expected to have one footpoint located. A green dotted curve indicates the nominal Parker spiral field line connecting to STEREO A's location, and demonstrates how the local field and SEPT apertures are located perpendicular to this direction. Near the Sun, purple ellipses with arrows indicate that electron beams are being injected onto these open field lines and propagating outwards towards STEREO A. As noted in the main text, since this population measured by SEPT occurs either side of the current sheet, electrons are likely being injected on both field lines. Lastly, grey solid arrows indicate the proposed flow velocity across the kink. The flow direction suggests the kink would wash over STEREO A's location over time, and that from left to right there is a rarefaction in wind speed (measured by STEREO A) which is a possible explanation for how such a magnetic field line shape could form.

Next, we discuss the solar wind context which advected over STEREO-A at the time it measured energetic electrons *in situ*. As mentioned in Section 3.3 the magnetic configuration measured by STEREO-A at the time of the energetic electron enhancement was un-

usual: While the nominal Parker spiral expectation is for the field to be oriented at either -45^o (anti-sunward) or $+135^o$ (sunward) in the RTN coordinate system in which the local radial direction is defined as 0^o, for this interval the field directions were near perpendicular to this at $+45^o$ first, then rotating by 180^o to $+135^o$. The SWEA measurements of the pitch angle distribution, and other information suggesting a solar origin for the solar wind measured stream, suggest the field line is not a closed loop but instead open with one footpoint tracing back to the Sun. To have a perpendicular-to-Parker configuration, the field line must therefore have a significant kink in it. The measured current sheet further complicates the picture by suggesting two streams of opposing polarity distorted in the same way. A schematic drawing suggesting a possible scenario is depicted in Figure 8 in which the field lines and current sheet are shown with a large kink in the vicinity of STEREO-A's location. The orientation of the STEREO-A SEPT Sun and Anti-Sun apertures are also illustrated, along with the direction of the electron strahl which determines the orientation of the kink in this cartoon. As time passes, this kink would advect out and over STEREO A, which would first measure the $+45^o$ inclined IMF, followed by a current sheet, followed by the -135^o inclined IMF. The longitudinal mapping of the field line would be affected by the presence of such a kink, with the size of the shift determined by the transverse scale of the kink. With the kink oriented in the sense shown here, the extra shift relative to the nominal Parker spiral is in fact Eastwards, which is the right direction to account for hte slight misalignment indicated in Figure 1. We see that the implied orientation of the current sheet would suggest that the $+45^o$ IMF maps to positive polarity in the corona, and the -135^o segment maps to negative polarity.

A plausible generation mechanism for such a kink (which is reminiscent of the switchbacks frequently observed by PSP, e.g. Bale et al. 2019; Kasper et al. 2019, but much larger scale) would be a velocity shear such as proposed by Schwadron & McComas (2021) leading to what those authors term the "super-Parker spiral". This is a simple effect of the distortion of a frozen-in Parker field line in the presence of a velocity shear. For the schematic shown in figure 8, the velocity shear is oriented as indicated by the size of the large gray arrows at the inflection points of the curve. This leads to the expectation that STEREO A would measure a gradual decrease in solar wind velocity with time as the kink washes over it, and indeed this is what is seen in the bottom panel of Figure 7.

Finally, we can comment on the implications of this sketched magnetic configuration for the interplanetary type III injection. As mentioned early, the energetic (55-85 keV) electrons measured by STEREO A/SEPT has an onset time of approximately 12:40 UT, rising as STEREO A crossed the current sheet and peaking around 13:30 UT before decaying away by 15:00 UT (all times on April 9 2019). Combined with our proposed schematic, we therefore interpret that there was a significant spread in field lines onto which the Type III noise storm was injecting electrons during time interval, including potentially on both sides of a polarity inversion line in the source active region. Given the event has an earlier onset than can be explained by the brightest type III at these times which we tracked in this work (see Figure 4), we suggest that there were other injections of energetic electrons onto interplanetary field lines that did not produce bright type III emission. LOFAR observations (Figure 4d) verify that such ubiquitous type III emission was occurring in the corona.

Given this near continuous emission (Cattell et al. 2020, found periodicities as rapid as 5 minutes) and the apparent connection between the start and end of the "perpendicular-to-Parker" stream and energetic electron populations in the STEREO-A data, this could indicate that throughout this time interval there are a lot of energetic electrons reaching 1 au, but the fortuitious alignment of a kink or other disturbance in the interplanetary field lines with the alignment of the STEREO-A SEPT apertures was required for these low flux events to be detected. We reiterate that although the onset of energetic electrons at STEREO-A cannot be explained by the event time of our specific event, the canonical arrival time ($\sim$19min) is consistent with the sharp rise in electron flux over this time, and given the non-Parker spiral configuration of the field line, the travel time is likely to be longer than this, meaning our event could feasibly be responsible for the peak in electron flux measured by SEPT at this time. In either case, we are confident that the population at SEPT is contributed to by our studied Type III event and thus we conclude that we have successfully traced an event from emission at the Sun out to 1 au in this work.

It is worth remarking that the association of *in situ* electron signatures with specific solar eruptive events is non-trivial in this case. In particular, we are unable to unambiguously associate a specific initial radio burst with the onset of the electrons at 12:40 UT. This situation contrasts with prior examples where clear linkage was observed, usually with more impulsive ($\mathcal{O}$(10 min)) electron enhancements (e.g., Klassen et al. 2011). For example, Krucker et al. (1999) studied 70 impulsive electron events and identified several directly traceable to specific type III bursts according to arrival time. Wang

et al. (2012) also showed a good statistical associated between energetic electron arrival and type III occurrence rate over a whole solar cycle. Krucker et al. (1999) and Haggerty & Roelof (2002) identified near-relativistic electron events for which the estimated release time of the electrons was delayed with respect to the onset of the type III radio bursts, but still found the electron event could be associated with a specific burst after accounting for this delay. Those authors suggested this delay indicates a separate population of electrons emitted later than those causing the radio waves (a prompt emission). This raises the possibility that in our case we are seeing delayed electron beams emitted from a range of type III bursts, including those where the radio brightness is small or not obviously interplanetary. Further, given the continuous enhancement over several hours, these individual injections most likely merged together for example via perpendicular diffusion (e.g., Strauss et al. 2017)

In closing, we have studied and tracked a non-flare related interplanetary Type III burst from its active region source, along open coronal field lines, along interplanetary field lines and shown evidence that it contributes to an energetic electron enhancement measured by STEREO-A at compatible times. A peculiar stream configuration at STEREO-A showed that the nominal Parker spiral connectivity is not necessarily needed for type III electrons to make it to 1au. To bring this story together we needed to make use of complementary observations including solar magnetograms, GOES X-ray observations, LOFAR ground based radio imaging observations, interplanetary radio dynamic spectra from widely separated interplanetary spacecraft and lastly, the powerful suite of *in situ* instruments on board STEREO A. This demonstrates the power of using the heliospheric systems observatory (HSO) for connecting the inner heliosphere and solar corona and demonstrates a useful future combination of techniques for tracking type III burst both for studying their intrinsic properties, as well as the convolved information they carry about the medium they propagate through. Since the launch of Solar Orbiter in 2020 (SO; Müller et al. 2020), there is a 4th source of interplanetary radio observations, leading to the possibility of extending the interplanetary part of this analysis to full 3D localization (i.e. relaxing the ecliptic confinement assumption), as well as giving another location in the heliosphere where *in situ* signatures could potentially be detected. Combined techniques as shown in this paper will therefore continue to become more capable and powerful as our instrumentaiton of the heliosphere continues to become more complete.

ACKNOWLEDGMENTS

Parker Solar Probe was designed, built, and is now operated by the Johns Hopkins Applied Physics Laboratory as part of NASA's Living with a Star (LWS) program (contract NNN06AA01C). The FIELDS experiment on PSP spacecraft were designed and developed under NASA contract NNN06AA01C. This work uses data from GONG, WIND, STEREO, LOFAR and GOES-15. The authors thank the mission and project teams and the Space Physics Data Facility for making the data publicly available. S.T.B was supported by NASA Mary W. Jackson Headquarters under the NASA Earth and Space Science Fellowship Program Grant 80NSSC18K1201. L.K.J thanks the support of the STEREO mission. D.L. acknowledges support from NASA Living With a Star (LWS) programs NNH17ZDA001N-LWS and NNH19ZDA001N-LWS, and the Heliophysics Innovation Fund (HIF) program. N.D. is grateful for support by the Turku Collegium for Science, Medicine and Technology of the University of Turku, Finland. E.C. is supported by the Schrödinger Fellowship at the Dublin Institute for Advanced Studies.

APPENDIX

1. TIME DELAY OF ARRIVAL (TDOA) TECHNIQUE

In this work, we utilized the time delay of arrival (TDOA; Alcock 2018) technique to derive the trajectory of the type III source region at heliospheric distance scales (i.e. large fractions of an au). In this appendix we explain the methodology used to derive these distance estimates.

At the top level, we take radio spectrogram data from three individual spacecraft (for the event studied in this work, Parker Solar Probe/FIELDS/RFS, STEREO-A/WAVES and Wind/WAVES) which are mutually separated by large enough distances (light travel time longer than several minutes and therefore longer than each instrument's time resolution). For each spacecraft we cut the spectrogram at a given frequency to obtain a time series of radio intensity at that wavelength, and then locate the peak of type III emission in that timeseries. To do this, we fit a 'flare profile' function (Gryciuk et al. 2017) which, although developed to explain the time profile of solar flare X-ray flux, also works very well for type III time profiles which have the same steep, near gaussian rise followed by an exponential tail. This gives us an absolute "time of arrival" at each space-

craft. Then, for each pair of spacecraft, we find the *difference* in time of arrival. Combining this with a baseline defined by the vector separation of the relevant spacecraft and assuming (1) free streaming radio emission from source to receiver and (2) near-ecliptic propagation of the burst, we can specify a single 2D hyperbola in the ecliptic plane along which the radio emission at that wavelength originates subject to the two assumptions above.

Obtaining such a hyperbola for two pairs of spacecraft (three spacecraft total) is sufficient to constrain the source position to a single point. Algorithmically, it results in two points, one sunward of the baseline and one anti-sunward, but we can rule out the anti-sunward source due to (1) the monotonically decreasing solar wind electron plasma density which prevent radio emission travelling inwards in the heliosphere, (2) simply that there are no credible alternatives to the canonical picture that type III bursts originate at the Sun.

Further, we can estimate a conservative error region by utilizing the instrument resolution for each spectrogram measurement. For PSP/RFS, S/WAVES and Wind/Waves these are 7s, 38.05d and 60s respectively, and should be summed to give an error in relative time of arrival between each pair. This is conservative since the time profiles of type III emission at a given wavelength are observed to be smooth profiles and we can fit to find the peak more accurately than the actual instrument resolution. The propagation to the source position effectively blurs the hyperbolae to give finite thickness. Intersecting these blurred profiles with three independent spacecraft measurements results in a hexagonal source region whose aspect ratio depends on relative spacecraft position (note that while the centroid is uniquely determined by two time delay measurements from three spacecraft, the error region is further constrained by including all permutations (three time delay measurements) from the three spacecraft. This hexagon can be found either by forming a minimum area convex hull from the analytic intersections of the edges of the blurred hyperbolae as illustrated in figure 9, or more simply as done in this paper by randomly sampling time delay measurements within the stated error bounds and populating the source positions in the ecliptic plane.

This source analysis method and error region formation process, similar to that presented by Alcock (2018), is summed up here in figure 9 for an example configuration with STEREO-A, STEREO-B and Wind in 2013. Here the time delays, noted on the plot in the same color as the relevant baseline are example values for illustrative purposes.

The remaining step to produce a full source trajectory as presented in the main text is to iterate this intersection process over frequency. In this work, we fit a smooth curve to each frequency (f) channel's peak flux timestamp (t), allowing inter-frequency interpolation since the channels in the different spacecraft are not precisely aligned. Specifically, we fit a second order polynomial function to the set of values ($1/f$,t), where we use the reciprocal of the frequency (wavenumber) since this results in a curve well approximated by a quadratic.

2. LONGER-TERM *IN SITU* CONTEXT

For further context and to support our intermediate conclusion that STEREO-A was connected back to the Sun at the time of interest, we zoom out to a longer time interval preceding and following the event in Figure 10. From top to bottom, this figure shows the pitch angle distribution of suprathermal electrons at 246.6 eV as measured by STEREO-A/SWEA (c.f. panel 4, Figure 7), the solar wind speed V, the solar wind proton density N_p, the solar wind proton temperature T_p, the magnetic field magnitude, the three components of the magnetic field vector in the spacecraft-centered RTN coordinate system, the magnetic field azimuth angle ϕ in RTN coordinates, the plasma β parameter, the total pressure P_t computed as the addition of the magnetic pressure plus the solar wind plasma thermal pressure, and the distribution of iron charge states Q_{Fe} as measured by STEREO-A/PLASTIC (Galvin et al. 2008). The red line in the T_p panel indicates the expected temperature according to the measured speed V following the expression by (Lopez 1987; Richardson & Cane 1995). The horizontal red and blue lines in the ϕ panel indicate the nominal Parker spiral azimuthal direction at -45° and 135°, i.e., the anti-sunward and sunward directions, respectively. The yellow shaded vertical bars as in Figure 7 and Figure 10 indicate the interval of perpendicular-to-Parker field lines during which the Type III burst of interest occurred.

From Figure 10, we see this structure was preceded by a stream interaction region (SIR) observed from 14:13 UT on April 7 to about ∼17:30 UT on April 8 that was accompanied by an increase of $\lesssim$1 MeV ion intensities as observed by STEREO-A/SEPT (not shown here). The stream interface of this SIR is indicated with the magenta dotted vertical line in Figure 10 and it was preceded by a weak forward shock at 14:13 UT on April 7 (blue vertical dotted line). Occurring more than 2 days in advance of our event, this structure is unlikely to have any bearing on the April 9th stream.

During the period of interest (yellow shaded bar), the distribution of iron charge states Q_{Fe} was slightly ele-

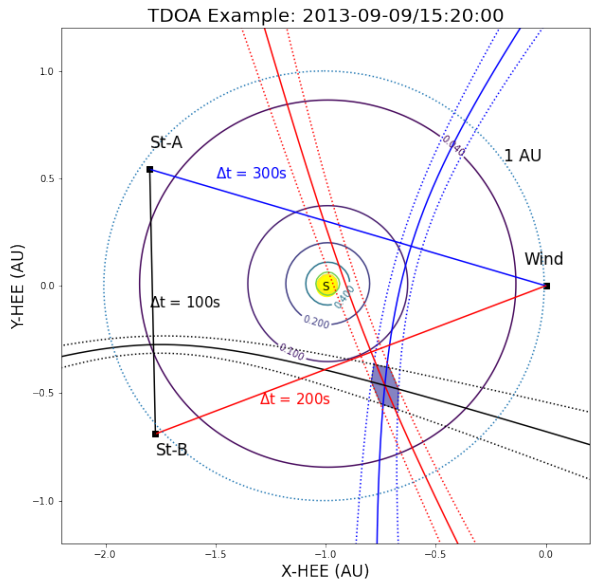

Figure 9. Schematic of the time delay of arrival localization method and associated error region. Here, a synthetic example is shown for a single frequency measurement applied to the constellation formed by STEREO A, STEREO B and Wind in September 2013. Each spacecraft's instantaenous position is labeled in the figure and the different baselines are drawn in different colors along with the time delay applied to that baseline. For each baseline and time delay "measurement" a hyperbola of constant arrival time is formed with a solid curve of the same color. Combining 2 or more of these solid curves a single (sunward) intersection point is found which is the burst position centroid. Additionally, error region hyperbolae are indicated for each measurement via dotted curves of the corresponding color. These are formed by maximizing the time delay error by combining instrument resolutions. As can be seen, the common intersecting envelope of these curves form a hexagon and, in contrast to the centroid, information is gained by including all three baselines in this analysis. Annotations on the plot also include the position of the Sun and contours showing the plasma frequency in MHz of a typical coronal density model (here, Saito et al. 1977). A dotted circle indicates 1 au where all three spacecraft in this constellation are approximately located.

vated and concentrated around values of 9-15, contrasting the ambient solar wind observed prior and after the passage of this peculiar structure. This suggests a different solar source for this region from the ambient solar wind (e.g. Lepri & Zurbuchen 2004).

Finally, despite the magnetic field orientation changes associated with the entry, current sheet and exit of STEREO A from the streams captured by the yellow shaded region, the plasma moments show the structure is not a typical flux rope. The magnetic field rotations are not smooth and the plasma β is high, thus they are both inconsistent with the canonical picture of flux ropes (e.g. Burlaga et al. 1982).

In summary, this wider analysis adds further evidence that the source of electron beams discussed in Section 3.3 are solar in origin.

REFERENCES

Acuña, M. H., Curtis, D., Scheifele, J. L., et al. 2008, SSRv, 136, 203, doi: 10.1007/s11214-007-9259-2

Alcock, B. T. 2018, PhD thesis, University of Glasgow, UK

Bale, S. D., Goetz, K., Harvey, P. R., et al. 2016, Space Science Reviews, 204, 49, doi: 10.1007/s11214-016-0244-5

Bale, S. D., Badman, S. T., Bonnell, J. W., et al. 2019, Nature, 576, 237, doi: 10.1038/s41586-019-1818-7

Bonnin, X., Hoang, S., & Maksimovic, M. 2008, A&A, 489, 419, doi: 10.1051/0004-6361:200809777

Bougeret, J. L., Kaiser, M. L., Kellogg, P. J., et al. 1995, SSRv, 71, 231, doi: 10.1007/BF00751331

Bougeret, J. L., Goetz, K., Kaiser, M. L., et al. 2008, SSRv, 136, 487, doi: 10.1007/s11214-007-9298-8

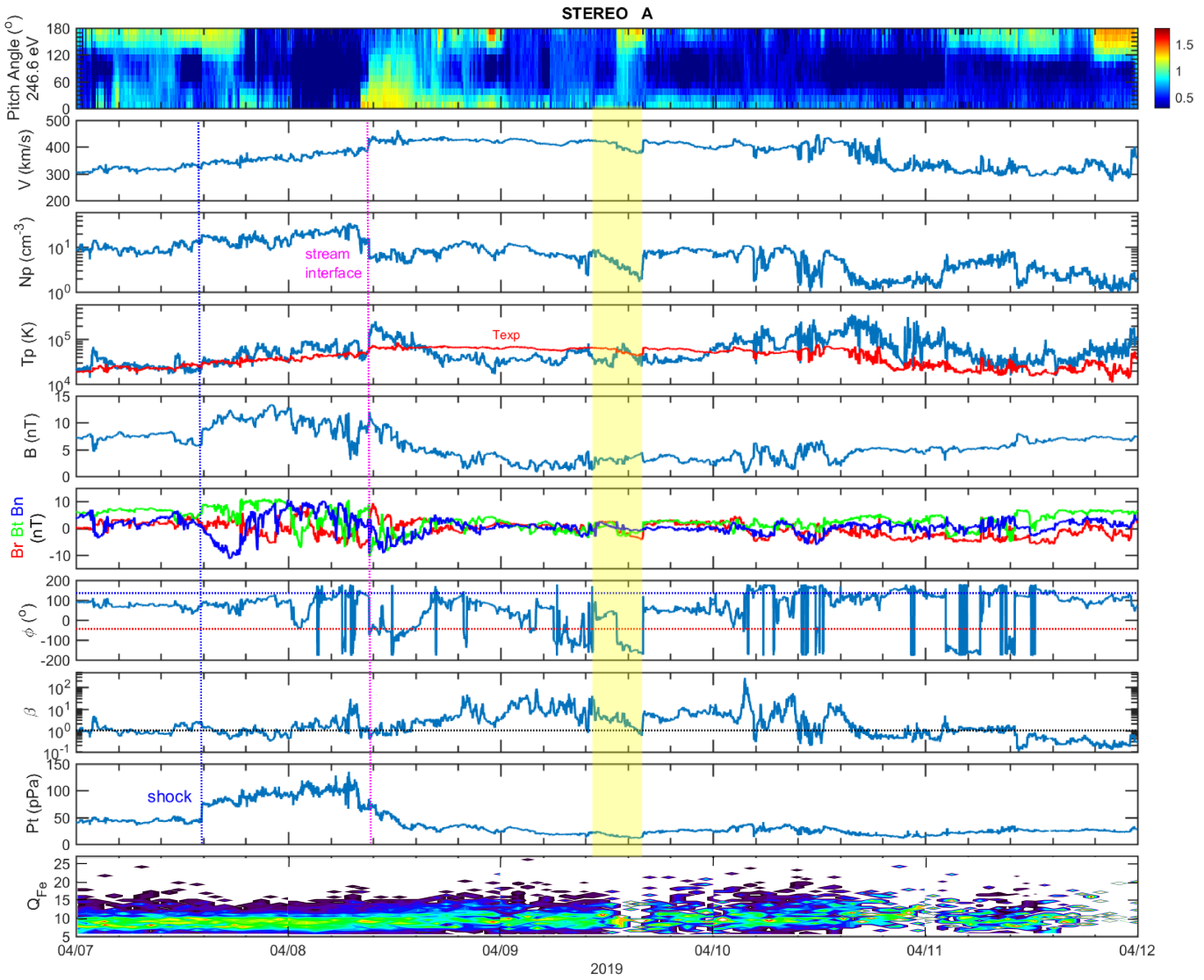

Figure 10. STEREO-A observations on 2019 April 7 - 11. From top to bottom: the pitch angle distribution of suprathermal electrons at 246.6 eV (color for the logarithm of phase space density), the solar wind speed V, solar wind proton density N_p, proton temperature T_p, magnetic field magnitude, the magnetic field vector in the spacecraft-centered RTN coordinate system, the magnetic field azimuth angle ϕ in RTN coordinates, the plasma β, the total pressure P_t, and the distribution of iron charge states Q_{Fe}. The red line in the T_p panel indicates the expected temperature according to the measured speed V. The blue and magenta dotted vertical lines denote the shock and stream interface, respectively. The yellow shaded area marks the period with peculiar magnetic field orientation.

Burlaga, L. F., Klein, L., Sheeley Jr., N. R., et al. 1982, Geophysical Research Letters, 9, 1317, doi: https://doi.org/10.1029/GL009i012p01317

Cattell, C., Glesener, L., Leiran, B., et al. 2020, arXiv e-prints, arXiv:2009.10899. https://arxiv.org/abs/2009.10899

Chamberlin, P. C., Woods, T. N., Eparvier, F. G., & Jones, A. R. 2009, in Society of Photo-Optical Instrumentation Engineers (SPIE) Conference Series, Vol. 7438, Solar Physics and Space Weather Instrumentation III, ed. S. Fineschi & J. A. Fennelly, 743802, doi: 10.1117/12.826807

Ergun, R. E., Larson, D., Lin, R. P., et al. 1998, ApJ, 503, 435, doi: 10.1086/305954

Fox, N. J., Velli, M. C., Bale, S. D., et al. 2016, Space Science Reviews, 204, 7, doi: 10.1007/s11214-015-0211-6

Galvin, A. B., Kistler, L. M., Popecki, M. A., et al. 2008, SSRv, 136, 437, doi: 10.1007/s11214-007-9296-x

Gryciuk, M., Siarkowski, M., Sylwester, J., et al. 2017, Solar Physics, 292, 77, doi: 10.1007/s11207-017-1101-8

Gurnett, D. A., & Anderson, R. R. 1976, Science, 194, 1159, doi: 10.1126/science.194.4270.1159

Haggerty, D. K., & Roelof, E. C. 2002, ApJ, 579, 841, doi: 10.1086/342870

Harra, L., Brooks, D. H., Bale, S. D., et al. 2021, arXiv e-prints, arXiv:2102.04964. https://arxiv.org/abs/2102.04964

Harvey, J. W., Hill, F., Hubbard, R. P., et al. 1996, Science, 272, 1284, doi: 10.1126/science.272.5266.1284

Kaiser, M. L. 2005, Advances in Space Research, 36, 1483, doi: 10.1016/j.asr.2004.12.066

Kasper, J. C., Bale, S. D., Belcher, J. W., et al. 2019, Nature, 576, 228, doi: 10.1038/s41586-019-1813-z

Klassen, A., Gómez-Herrero, R., & Heber, B. 2011, SoPh, 273, 413, doi: 10.1007/s11207-011-9735-4

Kontar, E. P., Chen, X., Chrysaphi, N., et al. 2019, apj, 884, 122, doi: 10.3847/1538-4357/ab40bb

Krucker, S., Larson, D. E., Lin, R. P., & Thompson, B. J. 1999, ApJ, 519, 864, doi: 10.1086/307415

Krupar, V., Maksimovic, M., Kontar, E. P., et al. 2018, ApJ, 857, 82, doi: 10.3847/1538-4357/aab60f

Krupar, V., Szabo, A., Maksimovic, M., et al. 2020, The Astrophysical Journal Supplement Series, 246, 57, doi: 10.3847/1538-4365/ab65bd

Leblanc, Y., Dulk, G. A., & Bougeret, J.-L. 1998, Solar Physics, 183, 165, doi: 10.1023/A:1005049730506

Lecacheux, A., Steinberg, J. L., Hoang, S., & Dulk, G. A. 1989, A&A, 217, 237

Lepri, S. T., & Zurbuchen, T. H. 2004, Journal of Geophysical Research (Space Physics), 109, A01112, doi: 10.1029/2003JA009954

Lin, R. P., Curtis, D. W., Larson, D. E., et al. 2008, SSRv, 136, 241, doi: 10.1007/s11214-008-9330-7

Liu, M., Issautier, K., Meyer-Vernet, N., et al. 2021, A&A, 650, A14, doi: 10.1051/0004-6361/202039615

Lopez, R. E. 1987, J. Geophys. Res., 92, 11189, doi: 10.1029/JA092iA10p11189

Melrose, D. B. 2017, Reviews of Modern Plasma Physics, 1, 5, doi: 10.1007/s41614-017-0007-0

Moncuquet, M., Meyer-Vernet, N., Issautier, K., et al. 2020, ApJS, 246, 44, doi: 10.3847/1538-4365/ab5a84

Müller, D., St. Cyr, O. C., Zouganelis, I., et al. 2020, A&A, 642, A1, doi: 10.1051/0004-6361/202038467

Müller-Mellin, R., Böttcher, S., Falenski, J., et al. 2008, SSRv, 136, 363, doi: 10.1007/s11214-007-9204-4

Musset, S., Maksimovic, M., Kontar, E., et al. 2021, A&A, 656, A34, doi: 10.1051/0004-6361/202140998

Newkirk, Gordon, J. 1961, ApJ, 133, 983, doi: 10.1086/147104

Offringa, A. R., McKinley, B., Hurley-Walker, N., et al. 2014, MNRAS, 444, 606, doi: 10.1093/mnras/stu1368

Pulupa, M., Bale, S. D., Bonnell, J. W., et al. 2017, Journal of Geophysical Research: Space Physics, 122, 2836, doi: 10.1002/2016JA023345

Pulupa, M., Bale, S. D., Badman, S. T., et al. 2020, The Astrophysical Journal Supplement Series, 246, 49, doi: 10.3847/1538-4365/ab5dc0

Reid, H. A. S., & Ratcliffe, H. 2014, Research in Astronomy and Astrophysics, 14, 773, doi: 10.1088/1674-4527/14/7/003

Richardson, I. G., & Cane, H. V. 1995, J. Geophys. Res., 100, 23397, doi: 10.1029/95JA02684

Saito, K., Poland, A. I., & Munro, R. H. 1977, Solar Physics, 55, 121, doi: 10.1007/BF00150879

Sauvaud, J. A., Larson, D., Aoustin, C., et al. 2008, SSRv, 136, 227, doi: 10.1007/s11214-007-9174-6

Schwadron, N. A., & McComas, D. J. 2021, ApJ, 909, 95, doi: 10.3847/1538-4357/abd4e6

Stansby, D., Yeates, A., & Badman, S. 2020, The Journal of Open Source Software, 5, 2732, doi: 10.21105/joss.02732

Steinberg, J. L., Hoang, S., Lecacheux, A., Aubier, M. G., & Dulk, G. A. 1984, aap, 140, 39

Strauss, R. D. T., Dresing, N., & Engelbrecht, N. E. 2017, ApJ, 837, 43, doi: 10.3847/1538-4357/aa5df5

Thejappa, G., & MacDowall, R. J. 2010, The Astrophysical Journal, 720, 1395. http://stacks.iop.org/0004-637X/720/i=2/a=1395

Thejappa, G., MacDowall, R. J., & Gopalswamy, N. 2011, The Astrophysical Journal, 734, 16. http://stacks.iop.org/0004-637X/734/i=1/a=16

van Diepen, G., Dijkema, T. J., & Offringa, A. 2018, DPPP: Default Pre-Processing Pipeline, Astrophysics Source Code Library, record ascl:1804.003. http://ascl.net/1804.003

van Haarlem, M. P., Wise, M. W., Gunst, A. W., et al. 2013, A&A, 556, A2, doi: 10.1051/0004-6361/201220873

Wang, L., Lin, R. P., Krucker, S., & Mason, G. M. 2012, ApJ, 759, 69, doi: 10.1088/0004-637X/759/1/69

Wild, J. P., & McCready, L. L. 1950, Australian Journal of Scientific Research A Physical Sciences, 3, 387, doi: 10.1071/CH9500387